Available online at www.sciencedirect.com

SciVerse ScienceDirect

Ceramics International 39 (2013) 2397–2404

CERAMICS INTERNATIONAL

www.elsevier.com/locate/ceramint

Effects of phase and chemical composition of precursor on structural and morphological properties of $(Lu_{0.95}Eu_{0.05})_2O_3$ nanopowders

N.A. Dulina[a,*], V.N. Baumer[a], M.I. Danylenko[b], P.V. Mateychenko[a], A.V. Tolmachev[a], O.M. Vovk[a], R.P. Yavetskiy[a]

[a]*STC ''Institute for Single Crystals'', NAS of Ukraine, 60 Lenin Ave., 61001, Kharkov, Ukraine*
[b]*Frantsevich Institute for Problems of Materials Science, NAS of Ukraine, 3 Krzhizhanovsky Str., 03680, Kyiv, Ukraine*

Received 6 August 2012; received in revised form 30 August 2012; accepted 30 August 2012
Available online 11 September 2012

Abstract

Europium-doped lutetium oxide nanopowders have been synthesized by the co-precipitation technique using ammonium hydrogen carbonate as a precipitant. Effects of chemical and phase composition of carbonate precursors on the morphology and sinterability of $(Lu_{0.95}Eu_{0.05})_2O_3$ nanopowders have been studied. Two types of precursors have been obtained differing by the molar ratio $R = NH_4HCO_3/Lu^{3+}$: a mixture of crystalline $Lu_{0.95}Eu_{0.05}(OH)(CO_3)\cdot 4H_2O$ and unidentified amorphous phases at $R = 4$–7 and crystalline $Lu_{0.95}Eu_{0.05}(H_2O)_x(HCO_3)_3\cdot nH_2O$ precursor at $R = 8$–20. The two-phase precursor consists of spherulite-like aggregates, while the crystalline one is characterized by plate-like morphology. Calcination of $Lu_{0.95}Eu_{0.05}(H_2O)_x(HCO_3)_3\cdot nH_2O$ leads to formation of $(Lu_{0.95}Eu_{0.05})_2O_3$ nanopowders that inherit the precursor morphology, while no morphology succession is observed for $(Lu_{0.95}Eu_{0.05})_2O_3$ nanopowders obtained by heat treatment of the two-phase precursor. Calcination of the two-phase mixture leads to breakdown of the spherulites and to formation of equiaxed particles with an average diameter of 40 nm with the standard deviation of particle size distribution of about 15%. The obtained low-agglomerated nanopowders were used in vacuum sintering to produce $(Lu_{0.95}Eu_{0.05})_2O_3$ optical ceramics with in-line transmittance of 41% at 611 nm.

Keywords: A. Powders: chemical preparation; B. Electron microscopy; E. Functional application; Lutetium oxide

1. Introduction

Significant achievements in the field of optical ceramics for photonics, optoelectronics, scintillation technique etc. are largely due to the development of advanced preparation technologies of weakly-agglomerated nanopowders [1]. In comparison with their micron-sized analogs, nanopowders show improved sinterability and provide better interaction of the nanoparticles ensemble during densification. This enables pressureless sintering of high-quality optical ceramics at reduced temperatures [2]. The main feature of nanopowders is their large specific surface, which favors surface diffusion of atoms. However, smaller particle size increases the agglomeration degree of nanopowders as well, which has the same driving force, the high surface curvature [3]. In fact, even low agglomeration of nanopowders results in translucent or even opaque ceramics due to residual pores which act as scattering centers. Thus, ensuring an optimized balance between sintering activity and agglomeration degree in processing of nanopowders is a key issue for advanced ceramic nanotechnologies.

Among numerous technologies for preparation of nanopowders, such as the sol–gel method [4,5], hydrothermal synthesis [6,7], flame spray pyrolysis [8] etc., chemical co-precipitation with subsequent calcination of precursor is considered as the most promising for preparation of highly-sinterable powders for optical ceramics [2]. Wet-chemical processes offer considerable advantages, such as easy mixing of the starting material and excellent chemical homogeneity of the final product [9]. As it is known, co-precipitation by ammonium hydrogen carbonate (AHC) results in formation of carbonate precursors possessing low thermal decomposition

---

*Corresponding author. Tel.: +380 057 341 0101;
fax: +380 057 340 9343.
E-mail address: dulina@isc.kharkov.ua (N.A. Dulina).

0272-8842/$ - see front matter © 2012 Elsevier Ltd and Techna Group S.r.l. All rights reserved.
http://dx.doi.org/10.1016/j.ceramint.2012.08.092

temperatures and only loose agglomeration [10–13]. Advantages of the use of carbonate precursors for synthesis of low-agglomerated nanopowders with high sinterability were reported for yttria and scandia [10,11], as well as for $Y_3Al_5O_{12}$ [2]. According to [12,13], carbonate precursors are promising as precipitants for preparation of active nanopowders of lutetium oxide (used as active media for solid-state lasers [14–17], ultrafast scintillators of ionizing radiation [18], transparent phosphors [19–22], etc).

The properties of oxide powder obtained by wet chemical methods are closely related to properties of its precursor, so, the properties of nanopowders are largely pre-determined during fabrication of the precipitant. In numerous works on synthesis of lutetium oxide by co-precipitation with AHC (or AHC-containing mixed precipitant) [13,23,24], no regularities relating chemical and phase composition of carbonate precursors with structural and morphological properties of Lu_2O_3 nanopowders have been established. In this work, we aimed at obtaining ~~of~~ co-precipitated $(Lu_{0.95}Eu_{0.05})_2O_3$ nanopowders with controlled structural and morphological characteristics by adjusting the precursor composition. $(Lu_{0.95}Eu_{0.05})_2O_3$ was chosen as a model system promising for scintillator application [19,20].

2. Experimental

$(Lu_{0.95}Eu_{0.05})_2O_3$ nanopowders were obtained by chemical co-precipitation using NH_4HCO_3 (AHC) as precipitant. Solutions of lutetium and europium chlorides were used as initial materials. The chlorides were prepared by dissolution of Lu_2O_3 and Eu_2O_3 (both of special purity grade) in concentrated hydrochloric acid with subsequent evaporation of excess acid. 1 M AHC solution was added to 0.1 M mother solution of rare earth chlorides. The precipitation process was carried out at room temperature; the drip rate was 1 ml/min. The molar ratio $R=NH_4HCO_3/Lu^{3+}$ was varied in the range of 4–20. The resultant suspension was kept for 24 h at room temperature with subsequent suction filtration. After repeated washing with deionized water and ethanol the precipitant was dried at 25 °C. $(Lu_{0.95}Eu_{0.05})_2O_3$ nanopowders were obtained by low-temperature calcination of the precursor for 2 h at 400–1100 °C. All synthesized nanopowders contained 5 at% of Eu^{3+} ions, which is optimum concentration to obtain the highest luminescence yield [19].

Phase identification was performed by X-ray diffraction (XRD) method on a SIEMENS D-500 X-ray diffractometer (CuKα radiation, graphite monochromator). The phases were identified using JCPDS PDF-1 card file and EVA retrieval system included in the diffractometer software. Rietveld refinement was performed with FullProf program [25]. An average apparent size of crystallites was calculated with FullProf using powder pattern of LaB_6 for obtaining of instrumental profile function. Morphology of the precursors and the nanopowders obtained was studied by scanning electron microscopy (JSM-6390LV, JEOL), transmission electronic microscopy (TEM-125, Selmi, Ukraine) and high-resolution analytical transmission electron microscopy (HR TEM, JEM-2100 F, JEOL). Differential thermal and thermogravimetric analyses of the precursor were carried out using a MOM Q-1500D derivatograph (Hungary). The heating rate was 10 °C/min, the alpha alumina was used as a reference. Specific surface area of the powders was determined by the Brunauer–Emmett–Teller (BET) method. An average particle size d_{BET} was determined assuming spherical particle shape from the following equation: $d_{BET}=6/\rho S_{BET}$, where ρ is the theoretical density of Lu_2O_3 (9.44 g/cm^3) and S_{BET} is the specific surface area. The particle size distribution was determined using a Zetasizer 1000HSA (Malvern Instruments, England) dynamic light scattering system. Shrinkage of $(Lu_{0.95}Eu_{0.05})_2O_3$ compacts was studied using a Netzsch-402 ED differential dilatometer in the 25–1450 °C temperature range with a heating rate of 10 °C/min. To produce $(Lu_{0.95}Eu_{0.05})_2O_3$ optical ceramics, the nanopowders were compacted into disks by the uniaxial pressing method and sintered at 1800–1850 °C for 15 h under 6×10^{-3} Pa vacuum. The samples were first heated to 1000 °C for 150 min and further to 1850 °C for 510 min. The resultant ceramics was 1 mm thick, polished on the both sides.

3. Results and discussion

3.1. XRD of carbonate precursor

It is known that pH value of the solution strongly affects the structural and morphological features of the precipitant formed. The molar ratio $R=NH_4HCO_3/Lu^{3+}$ is a conventional instrument to adjust pH value in the co-precipitation method. To study the pH influence on precursor properties, the water solution of lutetium chloride was precipitated by AHC within the $R=4$–20 range. The XRD patterns of the dried precursor synthesized at room temperature with 24 h ageing period are presented in Fig. 1. The phase composition of the precursor is strongly affected by R value. Diffraction patterns of precursors produced at $R=4$–7 and 8–20 (denoted as A and B, respectively) are quite different indicating that precipitants have different phase composition. The samples precipitated in the $R=4$–7 range are characterized by XRD

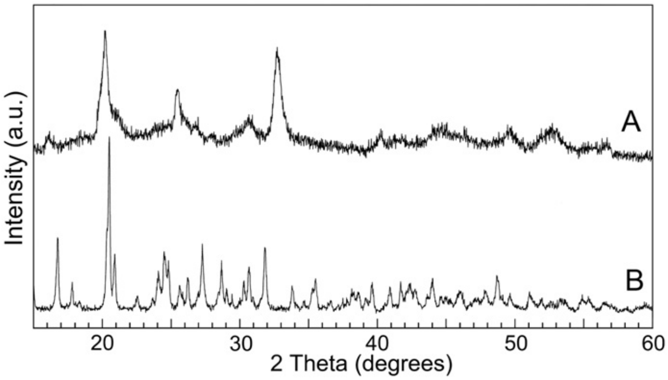

Fig. 1. XRD patterns of lutetium carbonate precursors synthesized in the $R=4$–20 range at room temperature and aged for 24 h.

patterns containing halo at 40–60 2θ° and several broadened diffraction peaks of low intensity. This may suggest that A precursor is biphasic, i.e., it is a mixture of crystalline and amorphous phases with relatively larger content of the latter. No halo and much more intense diffraction peaks with low half-width were found in the diffraction pattern of the B precursor. The XRD pattern of the precipitant obtained at $R=8$–20 is typical for the materials possessing high degree of crystallinity and structural perfection. Since there is no reliable data on the crystallographic structures of lutetium carbonates in the data-base of JCPDS, the phase composition of synthesized precursors was identified using literature data. Relative intensities and peak positions of A precursor in the XRD pattern are similar to those of basic lutetium carbonate reported in [26]. So we suggest that A precursor ($R=4$–7) consists of a mixture of crystalline $Lu_{0.95}Eu_{0.05}(OH)(CO_3)\cdot nH_2O$ and unidentified amorphous phases. XRD data of B precursor ($R=8$–20) are close to those described in [24], although the authors could not correctly identify the phase of complex lutetium carbonate. The crystal structure of B precursor correlates well with that of holmium carbonate [27]. Assuming that holmium and lutetium carbonates are isostructural due to close values of ionic radii, B precursor, probably, has the composition of $Lu_{0.95}Eu_{0.05}(H_2O)_x(HCO_3)_3\cdot nH_2O$.

Obviously the basic carbonate (A) and tris(hydrocarbonato) aquolutetium hydrate phases (B) are stable at the 4–7 and 8–20 ranges of the R value. NH_4HCO_3 solution contains several types of ionic species, such as NH_4^+, HCO_3^- and CO_3^{2-}. The composition of A precursor obtained at $R=4$–7 (pH < 7) is a result of competition between OH^- and carbonate species to form precipitates with Lu^{3+} by the following chemical reactions:

$$NH_4HCO_3 \leftrightarrow HCO_3^- + NH_4^+$$

$$HCO_3^- + OH^- \leftrightarrow CO_3^{2-} + H_2O$$

$$Lu^{3+} + Eu^{3+} + CO_3^{2-} + OH^- + 4H_2O \rightarrow Lu_{0.95}Eu_{0.05}(OH)(CO_3)\cdot 4H_2O,\ \text{at pH} \le 7\ (R=4\text{–}7) \quad (1)$$

At pH > 7 corresponding to the R values within the 8–20 range (Eq. (2)) NH_4HCO_3 hydrolysis via the first stage is predominant. The hydrolysis via the second stage is less pronounced. The HCO_3^- anion formed acts as a precipitating agent in the alkaline medium, resulting in formation of B precursor with approximate composition $Lu_{0.95}Eu_{0.05}(H_2O)_x(HCO_3)_3\cdot yH_2O$:

$$NH_4HCO_3 \leftrightarrow HCO_3^- + NH_4^+$$

$$Lu^{3+} + Eu^{3+} + HCO_3^- + (x+n)H_2O \rightarrow Lu_{0.95}Eu_{0.05}(H_2O)_x(HCO_3)_3\cdot nH_2O,\ \text{at pH} \ge 7\ (R=8\text{–}20) \quad (2)$$

3.2. Morphology of carbonate precursors

Since the size and morphology of the precursor particles are influenced by the growth conditions in the mother solution, the molar ratio R significantly affects the shape of the particles. Fig. 2 illustrates the morphologies of the samples obtained in the $R=4$–7 range (A precursor) and $R=8$–20 range (B precursor) as typical representatives for further analysis. Obviously, the particle morphology is composition dependent. The biphasic A precursor consists of plates joined into flower-like spherulites of 1–5 μm in diameter. Aggregates of similar morphology but slightly larger in diameter (up to ~30 μm) were obtained recently from 0.5 M mother solutions [24]. In our case, we suppose that the use of more diluted solutions as well as larger reaction volume prevents excessive agglomeration of the particles during precursor formation. The fully-crystalline B precursor synthesized at higher supersaturation ($R=8$–20) forms 10–15 μm rhombic plates consisting of strongly aggregated structural units. The mechanism of $Lu_{0.95}Eu_{0.05}(H_2O)_x(HCO_3)_3\cdot nH_2O$ precursor formation is probably related to physical adsorption phenomena. Under the action of Van der Waals attraction forces the primary structured particles are adjusted to each other and self-organized along the crystallographic axes to form a plate. Sodium bicarbonate $NaHCO_3$ is the simplest example of a crystalline precursor possessing plate-like rhombic morphology [28].

3.3. Thermal decomposition of carbonate precursors

Thermal behaviors of typical carbonate precursors studied by DTA/TG is shown in Fig. 3. The DTA curve of two-phase A precursor contains three extrema, namely, an intense endothermal peak at 160–320 °C, a weak endothermal peak at 420–500 °C, and a low-intensity exothermal

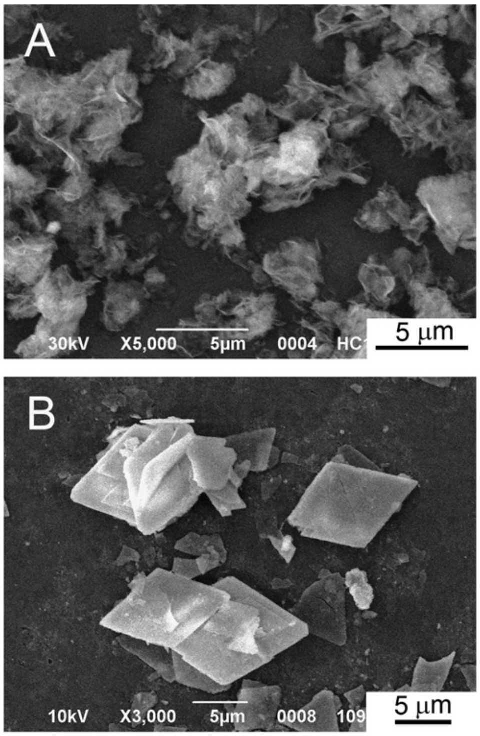

Fig. 2. SEM micrographs of lutetium carbonate precursors obtained in the $R=4$–7 range (A precursor) and $R=8$–20 range (B precursor).

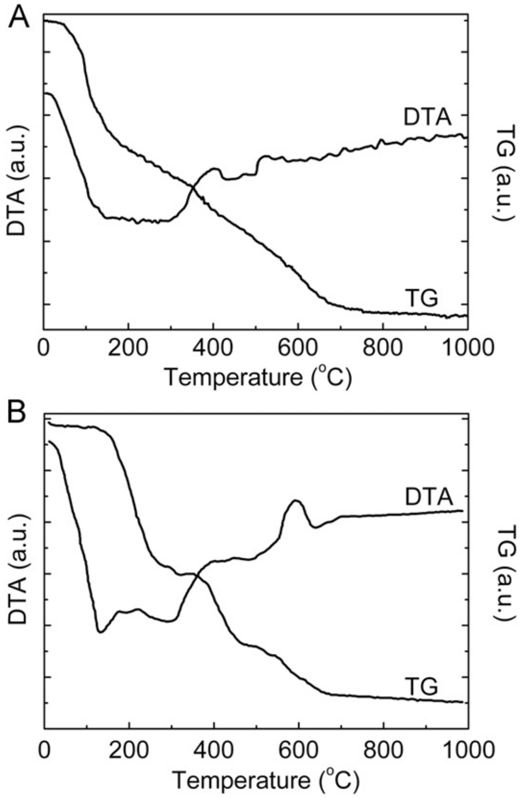

Fig. 3. DTA-TG traces of A (a) and B precursors (b), obtained at $R=4$–7 and $R=8$–20, correspondingly.

peak at 510–580 °C (Fig. 3a). Continuous weight loss of the sample is observed up to ~650 °C, making up 36% of the initial weight. The endotherms at $T=160$–320 °C and $T=420$–500 °C are due to removal of the adsorbed and constitution water, as well as decomposition of $(Lu_{0.95}Eu_{0.05})_2(CO_3)_3$ or $(Lu_{0.95}Eu_{0.05})_2O_2CO_3$ intermediates, respectively. The exotherm at $T=530$ °C corresponds to crystallization of lutetium oxide. According to the TG data, the composition of the precursor was taken as $Lu_{0.95}Eu_{0.05}(OH)(CO_3)\cdot 4H_2O$. Based on the results of thermal analysis, the phase composition evolution of A precursor during thermolysis may be described as follows:

$$Lu_{0.95}Eu_{0.05}(OH)(CO_3)\cdot 4H_2O \rightarrow Lu_{0.95}Eu_{0.05}(OH)(CO_3) \rightarrow (Lu_{0.95}Eu_{0.05})_2(CO_3)_3 \text{ or } (Lu_{0.95}Eu_{0.05})_2O_2CO_3 \rightarrow (Lu_{0.95}Eu_{0.05})_2O_3 \quad (3)$$

The proposed mechanism was found to be in a good agreement with decomposition of basic europium carbonate [29].

The thermal behavior of fully-crystalline B precursor is shown in Fig. 3b. The DTA curve reveals four extremums corresponding to endothermal and exothermal effects. The first intense endotherm at 130 °C corresponds to removal of the crystallization water, the second endothermal effect at 220–300 °C is due to decomposition of tris(hydrocarbonato)aquolutetium. The third weak endotherm observed in the temperature range of 450–570 °C corresponds to decomposition of intermediate lutetium carbonates. Finally, the relatively sharp exotherm at 590–630 °C with ~~a~~ maximum at 600 °C is related to crystallization of lutetium oxide. No thermal effects were observed on the DTA curve for the temperatures above 700 °C, which is in a good agreement with the TG data. Each thermal effect on the DTA curve is accompanied with simultaneous weight loss on the TG curve. The total weight loss was 35%. As it can be seen, $Lu_{0.95}Eu_{0.05}(H_2O)_x(HCO_3)_3\cdot nH_2O$ decomposes via three well-resolved stages followed by the formation of intermediate phases of unidentified composition. We failed to estimate the content of the constitution and crystallization water in lutetium crystalline hydrate $Lu_{0.95}Eu_{0.05}(H_2O)_x(HCO_3)_3\cdot nH_2O$, probably, due to the presence of molecular water. According to thermal behavior studies, B precursor decomposes in the following way:

$$Lu_{0.95}Eu_{0.05}(H_2O)_x(HCO_3)_3\cdot nH_2O \rightarrow Lu_{0.95}Eu_{0.05}(H_2O)_x(HCO_3)_3 \rightarrow Lu_{0.95}Eu_{0.05}(CO_3)_2 \rightarrow (Lu_{0.95}Eu_{0.05})_2O(CO_3)_2 \rightarrow (Lu_{0.95}Eu_{0.05})_2O_3 \quad (4)$$

3.4. Morphology of $(Lu_{0.95}Eu_{0.05})_2O_3$ nanopowders

To study the influence of the precursor phase and chemical composition on lutetium oxide morphology, the obtained A and B precipitates were calcined at $T=1000$ °C for 2 h. Despite close decomposition temperatures of both carbonate precursors (~700 °C, Fig. 3) and formation of the same cubic phase of lutetium oxide during crystallization, the morphology of the resulting $(Lu_{0.95}Eu_{0.05})_2O_3$ nanopowders is quite different. The TEM micrographs suggest that calcination of A precursor ($R=4$–7) leads to breakdown of the flakes and formation of the low-agglomerated equiaxed $(Lu_{0.95}Eu_{0.05})_2O_3$ particles of 40 nm in diameter and standard deviation of particle size distribution of 15% (Fig. 4a). According to our previous results [30], each particle is a single crystal since the selected area diffraction pattern from an isolated particle demonstrates only individual point reflections. The improved dispersity of the obtained powder is mainly due to the introduction of CO_3^{2-}, which is essential to obtain less agglomerated and uniformly dispersed powders. Release of CO_2 during the decomposition of the basic carbonate will prevent the particles from agglomerating with each other, thus resulting in weakly agglomerated $(Lu_{0.95}Eu_{0.05})_2O_3$ nanopowders. XRD analysis of the powders calcined at $T=1000$ °C for 2 h by the Rietveld method gives an average crystallite size equal to 35 nm. $(Lu_{0.95}Eu_{0.05})_2O_3$ nanopowders have the specific surface area of 16.1 m^2/g corresponding to ~39 nm particle size. A good agreement between mean particle sizes determined by XRD, TEM and BET methods indicates that resulting nanopowders are only slightly agglomerated and consist of near-isolated single crystalline particles. It seems that thermal decomposition of A precursor results in first-order-like phase transition. The discontinuous relief of mechanical stresses leads to transformation of the defect phase of the precursor (spherulites) into a family of structure-forming

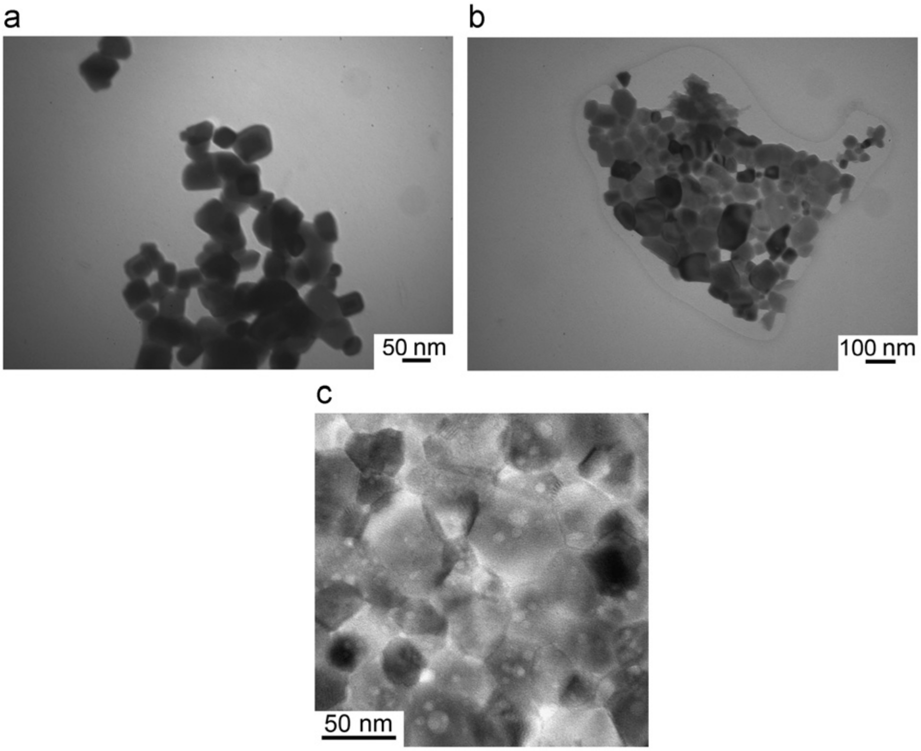

Fig. 4. TEM (a and b) and HRTEM (c) images of $(Lu_{0.95}Eu_{0.05})_2O_3$ nanopowders obtained by calcination of A (a) and B precursors (b and c) at $T = 1000$ °C for 2 h.

elements (homogenous nanoparticles with perfect crystal structure). Only calcination of powders at temperatures above 600 °C makes it possible to overcome the potential barrier and to turn the system into the stable state. Thus calcining of $Lu_{0.95}Eu_{0.05}(OH)(CO_3) \cdot 4H_2O$ precursor leads to complete disintegration of spherulite-like aggregates into well-dispersed individual particles indicating that there is no morphological inheritance between basic carbonate precursor and lutetium oxide. The same effect was recently observed for hydroxide- and carbonate-derived yttria nanopowders [10,31].

$(Lu_{0.95}Eu_{0.05})_2O_3$ nanopowders obtained by calcinations of B precursor ($R = 8$–20) inherit the morphology of its precursor due to incomplete collapse of the skeleton of the precursor particles (Fig. 4b and c). Dimensions of the micron-sized rhombic plates are 5×10 μm, while their thickness is equal to the diameter of primary particles (tens of nanometers). The similarity of morphologies of $Lu_{0.95}Eu_{0.05}(H_2O)_x(HCO_3)_3 \cdot nH_2O$ precursor and the resulting nanopowders seems to be related to the topotactic transition reaction during thermolysis [32]. The crystal structure of the oxide formed is related to that of its precursor by certain crystallographically equivalent, orientational relationships because there is a correspondence of several reflections near 21°, 34° and 44° in XRD pattern of cubic lutetia and its precursor (Fig. 1). Thermolysis of B precursor results in transformation of the plates into an aggregated skeleton of lamellar morphology consisting of primary lutetium oxide nanoparticles. According to XRD analysis by the Ritveld method $(Lu_{0.95}Eu_{0.05})_2O_3$ nanopowders have an average crystallite size of $d_{XRD} \sim 46$ nm while BET analysis reveals an average particle size of 65 nm (the specific surface area ~ 9.8 m^2/g). This means that europium-doped lutetium oxide nanopowders are aggregated to some degree. HRTEM micrograph points out that adjacent primary $(Lu_{0.95}Eu_{0.05})_2O_3$ particles with diameter in the range of 25–70 nm are joined to each other by common edges within the individual micron-sized plate.

The aggregation state of $(Lu_{0.95}Eu_{0.05})_2O_3$ nanopowders derived from different precursors was studied by the dynamic light scattering method. Particle size distributions of $(Lu_{0.95}Eu_{0.05})_2O_3$ nanopowders calcined at 1000 °C are shown in Fig. 5. The size of secondary aggregates of $(Lu_{0.95}Eu_{0.05})_2O_3$ A and B nanopowders significantly differs despite the close diameters of primary crystallites in the 55–70 nm range (Fig. 4). B nanopowders form micron-sized agglomerates whereas A powders possess narrow particle size distribution with the median particle size $D_{50} = 240$ nm (Fig. 5b) in a good agreement with the TEM data in Fig. 4. These results show that the dispersity of the resultant nanopowders is influenced not only by the agglomeration degree of the precursor particles but mainly by their chemical and phase composition. For instance, the agglomerated state of primary particles in A precursor (Fig. 2a) leads to only slightly agglomerated lutetium oxide nanopowders after calcination. Precise control of the chemical and phase composition of the precursor formed by co-precipitation method allows one to decrease the median particle size of $(Lu_{0.95}Eu_{0.05})_2O_3$ nanopowders by the factor of two compared with previously published data ($D_{50} = 458$ nm) [20]. However, agglomeration cannot

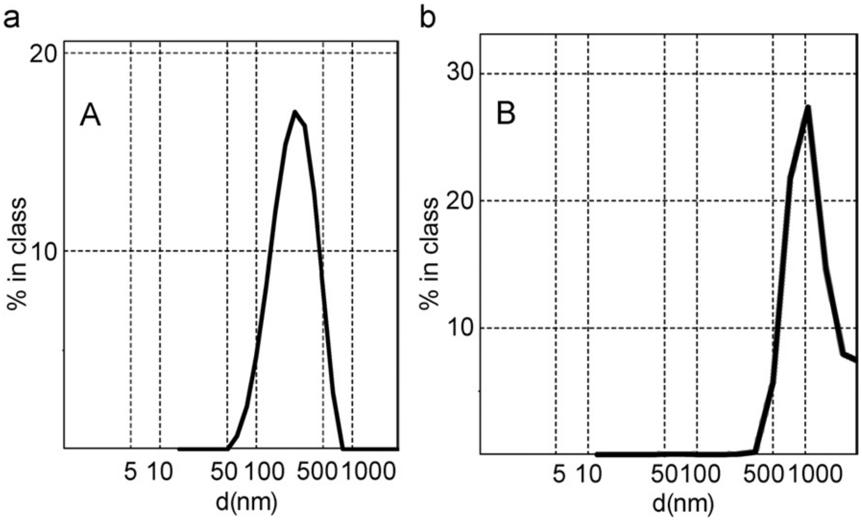

Fig. 5. Particle size distribution of $(Lu_{0.95}Eu_{0.05})_2O_3$ nanopowders obtained by calcination of A (a) and B precursors (b) at $T=1000$ °C for 2 h.

be suppressed completely since interparticle forces are very strong for particles less than 100 nm in size.

3.5. Sintering of $(Lu_{0.95}Eu_{0.05})_2O_3$ nanopowders

Sintering activity of nanopowders is strongly influenced by their structural and morphological characteristics. Therefore the distinctions in shape, size and aggregation degree of $(Lu_{0.95}Eu_{0.05})_2O_3$ A and B nanopowders may affect the final density and microstructure of the sintered ceramics. The densification behavior of europium-doped lutetia nanopowders was studied by sintering at a constant heating rate and by vacuum sintering methods. The linear shrinkage curves of nanopowders derived from different precursors are shown in Fig. 6. The initial density of $(Lu_{0.95}Eu_{0.05})_2O_3$ compacts was quite similar (~42–44% of the theoretical one) regardless of their aggregation state, while the character of density increase with temperature was quite different for A and B nanopowders. The shrinkage of A nanopowders starts at 800 °C, which is 200 °C lower as compared with B nanopowders. Further temperature rise results in intense densification of A nanopowders, and at 1450 °C the final density reaches ~90%. Excellent sintering activity of A nanopowders originates from high specific surface area (due to weak agglomeration), small size, and uniform morphology of the nanoparticles. After sintering by heating at constant rate up to 1450 °C the density of compacts from B nanopowders reaches ~63% and demonstrates a weak tendency to further increase.

Fig. 6b shows the densification rate for the nanopowders prepared from different precursors. The linear shrinkage rate $d(\Delta\rho/\rho_0)dt$ of A nanopowders is maximal when the temperature reaches 1450 °C, while B nanopowders densify most intensively at temperatures lower by ~250 °C. This can be explained by significant differences in the morphology and aggregate size of $(Lu_{0.95}Eu_{0.05})_2O_3$ nanoparticles. Highly-dispersed A nanopowders consist of isolated particles with relatively weak aggregation. Quite homogenous compact possessing uniform sintering can be fabricated from them. In contrast, B nanopowders containing micron-sized plate-like agglomerates show significant density gradients inside the green body owing to highly anisotropic morphology of the secondary aggregates. Sintering of B nanopowders starts at lower temperatures due to existence of large contact area between the nanoparticles within individual plate (Fig. 5c). It seems that at the initial stage occurs mainly 2D sintering due to high anisotropy of the rhombic aggregates forming two dimensional structures. Interagglomerate porosity suppresses densification of B nanopowders above 1250 °C, while

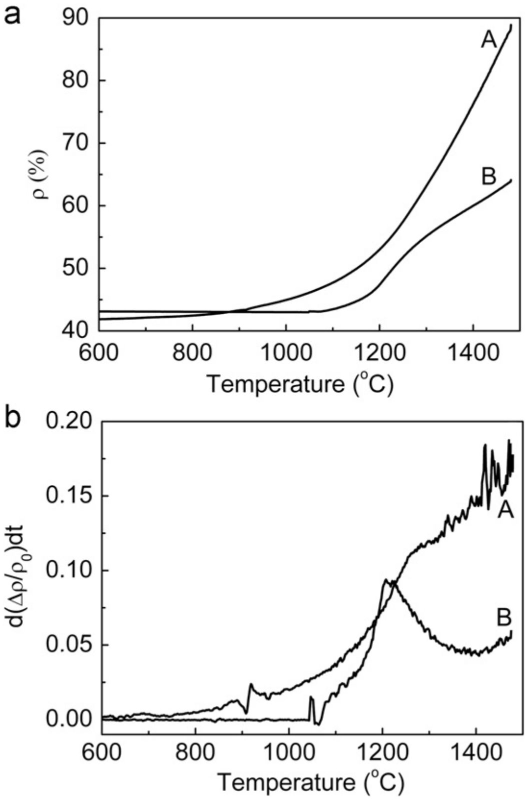

Fig. 6. Relative density versus temperature (a) and densification rate of $(Lu_{0.95}Eu_{0.05})_2O_3$ A and B nanopowders (b).

A nanopowders are still sintered in the whole temperature range studied.

Since $(Lu_{0.95}Eu_{0.05})_2O_3$ A nanopowders possess better structural and morphological uniformity and improved sinterability compared to B powders, they have been chosen as an object for further studies. The evolution of specific surface area and crystallite size of A nanopowders depending on the calcination temperature is presented in Fig. 7. The temperature increase from 600 to 1100 °C leads to specific surface area decrease from 37 down to 7 m^2/g (Fig. 7a). A drastic increase in average particle size d_{BET} estimated from BET values at the temperatures above 900 °C may be related to the formation of contacts between the neighboring particles and their coarsening via sintering. Thus the optimal temperature to produce near-discrete and well-dispersed $(Lu_{0.95}Eu_{0.05})_2O_3$ nanoparticles is $T=800$ °C. The dependences of the crystallite size and lattice parameter determined by Rietveld refinement method on the calcination temperature are shown in Fig. 7b. The rise of the precursor heat treatment temperature from 600 to 1100 °C results in the increase in the average crystallite size from 14 to 50 nm due to activation of mass transport. As the calcination temperature grows up, the lattice parameter of $(Lu_{0.95}Eu_{0.05})_2O_3$ nanopowders decreases, and the crystal structure of the powder becomes more perfect. However, even nanopowders calcined at 1100 °C have higher lattice constant compared to the theoretical value (10.4147 versus 10.3908 A, respectively) because of partial substitution of lutetium by bigger europium ions and higher defectivity of the nano-dimensional crystallites.

The established relationship between the phase and chemical composition of carbonate precursors and structural and morphological characteristics of europium-doped lutetium nanopowders was used to synthesize nanopowders with an optimal balance between the sintering activity and the degree of agglomeration. Fig. 8 shows $(Lu_{0.95}Eu_{0.05})_2O_3$ vacuum sintered optical ceramics prepared from A nanopowders at 1850 °C for 15 h. The ceramics is characterized by 99.5% density, 50 μm average grain size, and 41% in-line transmittance at 611 nm for 1 mm thick specimen [33]. It should be noted that under the sintering conditions studied B nanopowders give only opaque ceramics. Further progress in improvement of ceramics optical quality is expected with colloidal compaction approaches [34]. These methods allow to use the interparticle forces for the formation of homogenous high-density compacts by self-organization of nanoparticles [3].

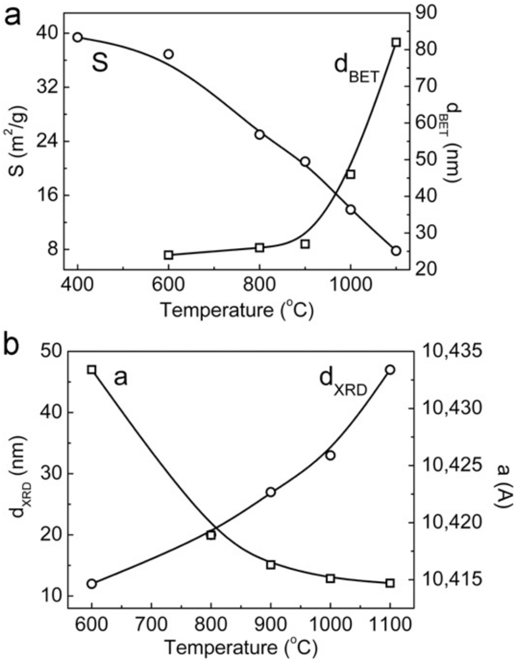

Fig. 7. Specific surface area, average particles size (a) and average crystallite size and lattice constant (b) of $(Lu_{0.95}Eu_{0.05})_2O_3$ A nanopowders versus calcinations temperature.

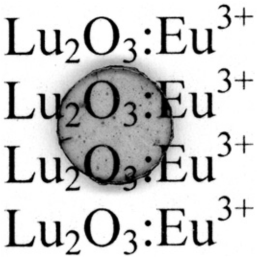

Fig. 8. $(Lu_{0.95}Eu_{0.05})_2O_3$ ceramics obtained by vacuum sintering of A nanopowders at 1850 °C for 15 h.

4. Conclusions

Two types of precursors have been obtained with different molar ratios $R=NH_4HCO_3/Lu^{3+}=4$–20, i.e., $Lu_{0.95}Eu_{0.05}(OH)(CO_3)\cdot 4H_2O$ ($R=4$–7) and $Lu_{0.95}Eu_{0.05}(H_2O)_x(HCO_3)_3\cdot nH_2O$ ($R=8$–20). The sintering activity and agglomeration degree of $(Lu_{0.95}Eu_{0.05})_2O_3$ nanopowders were found to be strongly affected not only by structural and morphological characteristics of precursors but also by their chemical and phase composition. Calcination of diphase precursor containing a mixture of crystalline $Lu_{0.95}Eu_{0.05}(OH)(CO_3)\cdot 4H_2O$ and unidentified amorphous phases at 1000 °C results in formation of equaxed $(Lu_{0.95}Eu_{0.05})_2O_3$ particles of low agglomeration degree with the average particle size ~40 nm and standard deviation of 15%. $(Lu_{0.95}Eu_{0.05})_2O_3$ nanopowders prepared by calcination of $Lu_{0.95}Eu_{0.05}(H_2O)_x(HCO_3)_3\cdot nH_2O$ precursor inherit its morphology and form plate-like aggregates of primary nanoparticles with dimensions of 5 × 10 μm. It has been determined that $(Lu_{0.95}Eu_{0.05})_2O_3$ nanopowders obtained from the biphasic precursor possess improved morphological and structural characteristics and higher sintering activity in comparison with those prepared from the crystalline precursor, densifying into transparent ceramics after vacuum sintering at 1850 °C for 15 h.

Acknowledgments

This work was partially supported by RFBR Project 11-02-90465-Ukr_f_a and SFFR Project F40.7/061. The authors would like to acknowledge A.G. Doroshenko, A.V. Ragulya for the help in testing of experimental samples.

References

[1] G.L. Messing, A.J. Stevenson, Toward pore-free ceramics, Science 322 (2008) 383–384.

[2] J. Lu, K. Ueda, H. Yagi, et al., Neodymium doped yttrium aluminum garnet ($Y_3Al_5O_{12}$) nanocrystalline ceramics—a new generation of solid state laser and optical materials, Journal of Alloys and Compounds 341 (2002) 220–225.

[3] A. Krell, H.-W. Ma, Sintering transparent and other sub-μm alumina: the right powder, CFI/Berichte der Deutschen Keramischen Gesellschaft 80 (2003) E41–E45.

[4] E. Zych, J. Trojan-Piegza, L. Kępiński, et al., Microstructure and spectroscopy of Lu_2O_3:Eu prepared using various synthesis techniques, Solid State Phenomena 99–100 (2004) 25–30.

[5] L. Li, H.K. Yang, B.K. Moon, et al., Photoluminescent properties of Ln_2O_3:Eu^{3+} (Ln = Y, Lu and Gd) prepared by hydrothermal process and sol–gel method, Materials Chemistry and Physics 119 (2010) 471–477.

[6] M.K. Devaraju, S. Yin, T. Sato, Tm^{3+}-doped Y_2O_3 nanocrystals: rapid hydrothermal synthesis and luminescence, European Journal of Inorganic Chemistry 29-30 (2009) 4441–4445.

[7] D. Zhou, Y.Y. Ren, Y. Shi, et al., Hydrothermal synthesis of fully crystalline Nd:Lu_2O_3 nanopowders under a low temperature, Journal of Alloys and Compounds 504 (2010) L36–L38.

[8] C. Baker, W. Kim, J. Sanghera, et al., Flame spray synthesis of Lu_2O_3 nanoparticles, Materials Letters 66 (2012) 132–134.

[9] W. Kim, C. Baker, G. Villalobos, et al., Synthesis of high purity Yb^{3+}-doped Lu_2O_3 powder for high power solid-state lasers, Journal of the American Ceramic Society 94 (9) (2011) 3001–3005.

[10] N. Saito, S. Matsuda, T. Ikegami, Fabrication of transparent yttria ceramics at low temperature using carbonate-derived powder, Journal of the American Ceramic Society 81 (1998) 2023–2028.

[11] J.-G. Li, T. Ikegami, T. Mori, et al., Wet-chemical routes leading to Scandia nanopowders, Journal of the American Ceramic Society 86 (2003) 1493–1499.

[12] Z. Wang, W. Zhang, B. You, et al., Effects of precipitant on microstructure and luminescent properties of Lu_2O_3:Eu^{3+} nanopowders and ceramics, Spectrochimica Acta, Part A 70 (2008) 835–839.

[13] D. Zhou, Y. Shi, P. Yun, et al., Influence of precipitants on morphology and sinterability of Nd^{3+}:Lu_2O_3 nanopowders by a wet chemical processing, Journal of Alloys and Compounds 479 (2009) 870–874.

[14] J. Lu, K. Takaichi, T. Uematsu, et al., Promising ceramic laser material: highly transparent Nd^{3+}:Lu_2O_3 ceramic, Applied Physics Letters 81 (2002) 4324–4326.

[15] K. Takaichi, H. Yagi, A. Shirakawa, et al., Lu_2O_3:Yb^{3+} ceramics—a novel gain material for high-power solid-state lasers, Physica Status Solidi A 202 (2005) R1–R3.

[16] L. An, A. Ito, T. Goto, Effects of ball milling and post-annealing on the transparency of spark plasma sintered Lu_2O_3, Ceramics International 37 (2011) 2263–2267.

[17] J. Sanghera, W. Kim, C. Baker, et al., Laser oscillation in hot pressed 10% Yb^{3+}:Lu_2O_3 ceramic, Optical Materials 33 (2011) 670–674.

[18] T. Yanagida, Y. Fujimoto, S. Kurosawa, Ultrafast transparent ceramic scintillators using the Yb^{3+} charge transfer luminescence in RE_2O_3 host, Applied Physics Express 4 (2011) 126402-1-3.

[19] A. Lempicki, C. Brecher, P. Szupryczynski, et al., A new lutetia-based ceramic scintillator for X-ray imaging, Nuclear Instruments and Methods in Physics Research, Section A 488 (3) (2002) 579–590.

[20] Q. Chen, Y. Shi, L. An, et al., Fabrication and photoluminescence characteristics of Eu^{3+}-doped Lu_2O_3 transparent ceramics, Journal of the American Ceramic Society 89 (2006) 2038–2042.

[21] Y. Shi, Q.W. Chen, J.L. Shi, Processing and scintillation properties of Eu^{3+} doped Lu_2O_3 transparent ceramics, Optical Materials 31 (2009) 729–733.

[22] Z.M. Seeley, J.D. Kuntz, N.J. Cherepy, et al., Transparent Lu_2O_3:Eu ceramics by sinter and HIP optimization, Optical Materials 33 (2011) 1721–1726.

[23] Q. Chen, Y. Shi, L. An, et al., A novel co-precipitation synthesis of a new phosphor Lu_2O_3:Eu^3, Journal of the European Ceramic Society 27 (2007) 191–197.

[24] X. Li, X. Sun, Li Ji-G., et al., Synthesis of Nano-Sized Lu_2O_3 powder for transparent ceramics fabrication using carbonate derived precursors, in: D. Jiang, Y. Zeng, M. Singh, J. Heinrich (Eds.), Ceramic Materials and Components for Energy and Environmental Applications, Wiley, New-York, 2010, pp. 597–603.

[25] J. Rodriguez-Carvajal, T. Roisnel, FullProf.98 and WinPLOTR: new Windows 95/NT applications for diffraction commission for powder diffraction, IUCr Newsletter 20 (1998).

[26] S. Liu, R-J. Ma, Synthesis of hydrated lutetium carbonate, Acta Chemica Scandinavica 51 (1997) 893–895.

[27] W.J. Rohrbaugh, R.A. Jacobson, Crystal and molecular structure of the decacoordinate complex tris(bicarbonato)tetraaquoholmium(III) dihydrate, $Ho(H_2O)_4(HCO_3)_3(H_2O)_2$, Inorganic Chemistry 13 (1974) 2535–2539.

[28] E.A. Prodan, General Regularities of the Thermal Decomposition of Crystalline Inorganic Compounds, Institute of Chemistry, Plotsk, 1979 (in Russian).

[29] N.V. Mazereushvili, V.P. Natidze, E.N. Zedelashvili, About europium carbonates, Communications of the Georgian SSR Academy of Sciences 72 (1973) 345–348 (in Russian).

[30] N.V. Babayevskaya, T.G. Deyneka, P.V. Mateychenko, et al., Fabrication and characterization of Lu_2O_3:Eu^{3+} nanopowders and X-ray films, Journal of Alloys and Compounds 507 (2010) L26–L31.

[31] T. Ikegami, J.-G. Li, T. Mori, et al., Fabrication of transparent yttria ceramics by the low-temperature synthesis of yttrium hydroxide, Journal of the American Ceramic Society 85 (2002) 1725–1729.

[32] P.P. Fedorov, V.V. Voronov, V.K. Ivanov, et al., Evolution of yttria nanoparticle ensembles, Nanotechnologies in Russia 5 (2010) 624–634.

[33] N.A. Dulina, Yu.L. Kopylov, V.B. Kravchenko, et al., Fabrication and characterization of Eu^{3+}-doped Lu_2O_3 scintillation ceramics, Optical Materials. http://dx.doi.org/10.1016/j.optmat.2012.04.020.

[34] N.A. Dulina, T.G. Deineka, R.P. Yavetskiy, et al., Comparison of dispersants performance on the suspension Lu_2O_3:Eu^{3+} stability and high-density compacts on their basis, Ceramics International 37 (2011) 1645–1651.